Volume 12
Number 48
28 December 2020
Pages 24299-24546

Nanoscale

rsc.li/nanoscale

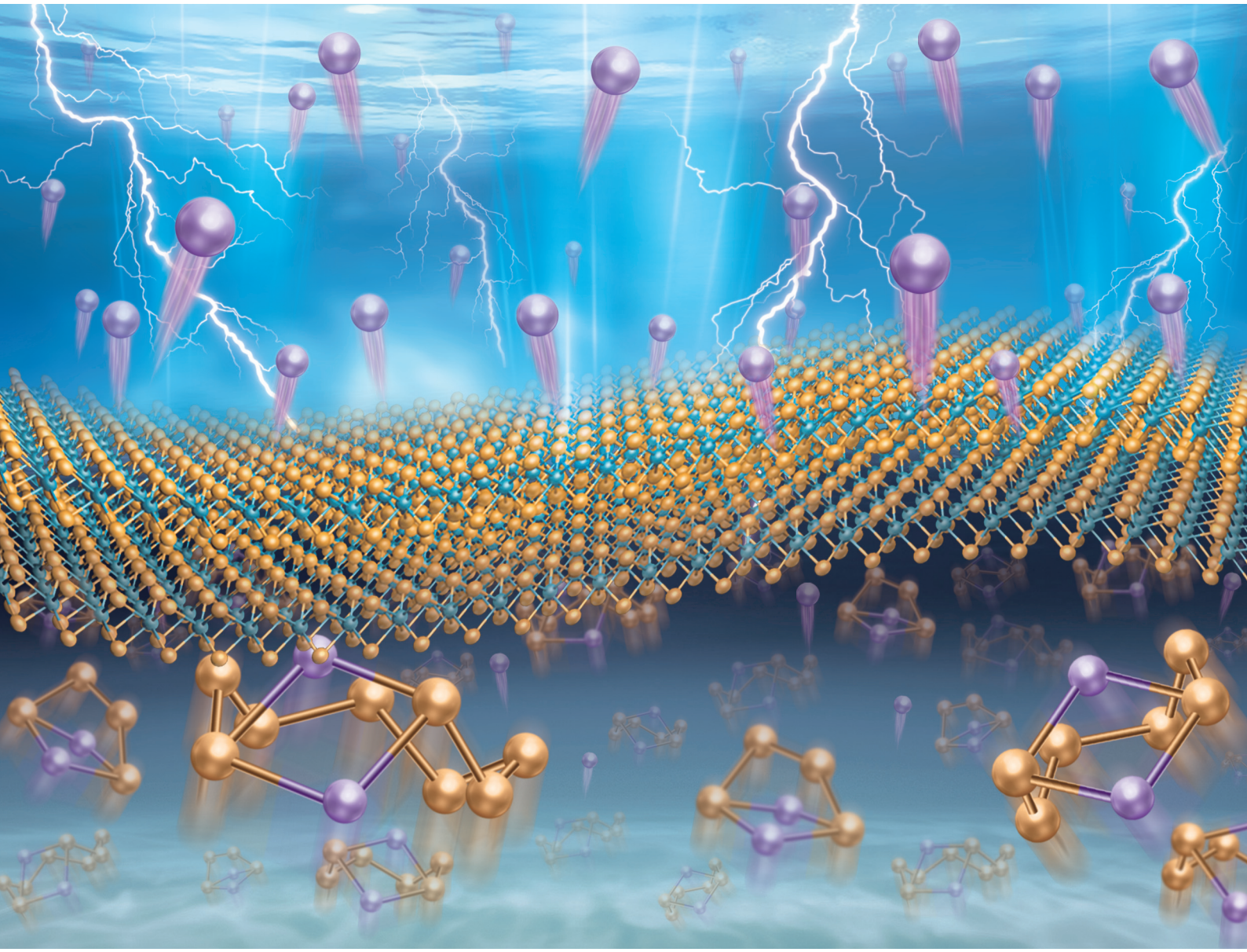

ISSN 2040-3372

ROYAL SOCIETY OF CHEMISTRY

PAPER
Linfei Lai, Da Zhan *et al.*
A TiS_2/Celgard separator as an efficient polysulfide shuttling inhibitor for high-performance lithium–sulfur batteries

NCNST

Nanoscale

ROYAL SOCIETY OF CHEMISTRY

PAPER

View Article Online
View Journal | View Issue

Check for updates

Cite this: *Nanoscale*, 2020, **12**, 24368

A TiS_2/Celgard separator as an efficient polysulfide shuttling inhibitor for high-performance lithium–sulfur batteries†

Guanfusheng Yan,[a,b,c] Chuan Xu,[a] Zhaohui Meng,[a] Mingzhen Hou,[c] Wen Yan,[a] Naibo Lin,[a] Linfei Lai *[c,d] and Da Zhan*[a,b]

Received 6th September 2020,
Accepted 26th September 2020

DOI: 10.1039/d0nr06429g

rsc.li/nanoscale

The rapid capacity loss caused by the shuttling effect of polysulfides is one of the great challenges of Li–S batteries. In this work, we adopted a simple solid-phase sintering method to synthesize titanium disulfide (TiS_2) and further demonstrated it as a superior modifier of separators for Li–S batteries. Two commonly adopted modification processes of separators, including vacuum filtration (VF) and slurry casting (SC) have been used to prepare TiS_2/Celgard separators. TiS_2-VF/Celgard can better restrain the polysulfide shuttling effect compared with TiS_2-SC/Celgard. A TiS_2-VF/Celgard-based Li–S battery has a reversible capacity of 771.6 mA h g^{-1}, with a capacity retention of 645.6 mA h g^{-1} after 500 cycles at 2.0 C, corresponding to a capacity fading rate of ~0.033% per cycle. This study has shown the potential of TiS_2 as a multifunctional modifier of separators for high performance and long cycle life Li–S batteries.

1. Introduction

Lithium–sulfur (Li–S) batteries have become a current research focus due to their high theoretical capacity (1675 mA h g^{-1}), high energy density (2600 W h kg^{-1}), eco-friendliness, low cost of the sulfur element, and abundant natural reserves.[1,2] However, there are still some issues obstructing the commercialization of Li–S batteries, among them, the shuttle effect of polysulfide intermediates (Li_2S_x, $4 \leq x \leq 8$) is considered to be the most important one.[3] The polysulfide intermediates produced by the positive electrode easily dissolve in the electrolyte, pass through the separator, and diffuse to the negative electrode, thereby directly reacting with the lithium anode, which rapidly reduces the capacity value, cycle life, and Coulomb efficiency of the Li–S battery.[4–6] In recent years, many strategies have been applied to overcome the shuttling effect of lithium polysulfides (PSs) and improve the cycling stability of Li–S batteries, such as electrode structure modulation, electrolyte system innovation, and separator modification.[7,8]

Commercial lithium battery separators are mainly polyolefin porous membranes such as polyethylene (PE) and polypropylene (PP) with pore sizes in the range between ~30 and 100 nm, facilitating the fast diffusion of ions.[9] The conventional separator has a pore size significantly larger than that of PSs, which leads to a rapid loss of electroactive materials once PSs escape from the porous cathode and dissolves in the electrolyte.[10] Therefore, a cation-selective separator that efficiently impedes the PS anion shuttling between the cathode and anode will be of great significance for Li–S batteries.[11]

2D graphene or graphene oxide has been reported as a high-performance modification layer for conventional battery separators.[12] Nevertheless, non-polar carbon has limited physical adsorption capacity to immobilize polar PSs;[13–15] the PSs are still prone to dissolve in the electrolyte and result in a fast capacity loss. Therefore, polar oxides,[16,17] sulfides,[18] covalent organic frameworks (COFs),[19] and carbides have been explored as the modification layer of separators with higher PS affinity than carbon layers[20] to improve the stability of Li–S batteries. Besides graphene and boron nitride, transition metal dichalcogenides (TMDs) are among the most studied ultrathin materials. In particular, titanium disulfide (TiS_2) is popular in both fundamental research and industry due to its unique physical properties,[21] high electrical conductivity, and abundant transition metal d orbital electrons.[22] Meso/micro porous materials provide structural confinement of PSs. Micrometer size pore-free TiS_2 as a Li–S battery cathode has shown an

[a]Research Institution for Biomimetics and Soft Matter, Fujian Key Provincial Laboratory for Soft Functional Materials Research, College of Materials, Xiamen University, Xiamen, 361005, China. E-mail: zhanda@ciomp.ac.cn
[b]State Key Laboratory of Luminescence and Applications, Changchun Institute of Optics, Fine Mechanics and Physics, Chinese Academy of Sciences, Changchun 130033, China
[c]Key Laboratory of Flexible Electronics (KLOFE) & Institute of Advanced Materials (IAM), Nanjing Tech University (Nanjing Tech), Nanjing, 211816, China
[d]CINTRA CNRS/NTU/Thales, UMI 3288, 50 Nanyang Drive, 637553, Singapore. E-mail: linfei.lai@ntu.edu.sg

†Electronic supplementary information (ESI) available. See DOI: 10.1039/d0nr06429g

improved cycle life,[23] which is comparable to those of nanoporous carbon-based electrodes. Theoretical calculations and experimental results have validated that TiS_2 has a strong surface affinity to PSs.[24] Despite the advantages of using TiS_2 as electrodes, benefiting from its unique physical properties, there are very limited reports on TiS_2 derived from a facile solvent-free sintering method as a modification layer of separators for various types of Li–S batteries, regardless of the electrode materials used. Pan *et al.*[25] utilized a conventionally widely adopted chemical method to synthesis TiS_2 for the modification of separators. Although its electrochemical performance has been well investigated, the effect of the modification process has not been studied in-depth. Huang *et al.*[26] reported the synthesis of TiS_2 confined within N,S co-doped porous carbon from $Ti_3C_2T_x$ as a freestanding sulfur cathode for Li–S batteries. In order to prepare high-quality TiS_2 sheets, the $Ti_3C_2T_x$ precursor has been treated by HF acid etching, delamination, and freeze-drying followed by thermal annealing, which involved time-consuming multistep processes.

Herein, in our work, we have synthesized high-quality TiS_2 by a solid-phase sintering method, which is scalable and time-saving, and we further demonstrated its PS immobilization properties as a modification layer of commercially available Celgard separators. As a barrier layer, TiS_2 modified Celgard (TiS_2/Celgard) can efficiently prevent the shuttling of PSs from the cathode to the anode side, and lead to high capacity retention in long cycle life. The separator modification processes with TiS_2 in vacuum filtration (TiS_2-VF/Celgard), and slurry coating (TiS_2-SC/Celgard) have been systematically evaluated and rigorously compared. TiS_2-VF/Celgard has shown higher Li^+ conductivity and could better immobilize PSs than TiS_2-SC/Celgard-based Li–S battery devices (Fig. 1).

2. Experimental

Materials and chemicals

All commercial chemicals were used as purchased unless stated otherwise, including sublimed sulfur (S, 99.999%, Aladdin), titanium powder (Ti, 99 wt%), ethanol (C_2H_5OH, >99.5%, Sinopharm Chemical Reagent Co., Ltd), 1-methyl-2-pyrrolidone (NMP ≥ 99%, Sinopharm Chemical), polyvinylidene fluoride (PVDF), Ketjen Black (EC-600JD), lithium sulfide (Li_2S), polyvinylpyrrolidone (PVP), and Super P carbon black.

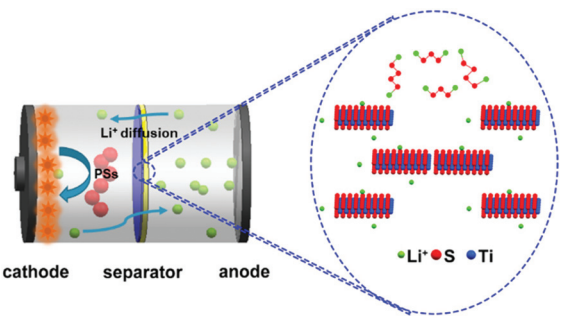

Fig. 1 Schematic of Li–S batteries with the TiS_2/Celgard separator.

Synthesis of TiS_2

TiS_2 was prepared by a one-step solid-phase sintering method. Sulfur powder and titanium powder were mixed in a molar ratio of 2 : 1 in a quartz tube, then the tube was pumped to create a vacuum state and sealed. The sealed tube was then annealed at 660 °C in a tube furnace (ramping rate: 5 °C min^{-1}). After the tube furnace cooled down naturally, the sample was collected from the quartz tube and further crushed into powder in a glove box. The collected sample was added to 5 mL carbon disulfide (CS_2), and dried naturally and stored in a glove box.

Preparation of the modified separator

TiS_2-VF/Celgard prepared by vacuum filtration: firstly, 0.5 g PVP, 35 mg TiS_2 and an appropriate amount of PVDF were dispersed in NMP to form a homogeneous slurry. After sonication for 2 h and stirring for 6 h, the mixed slurry was added into a vacuum filter bottle using a pipette and filtered through a Celgard membrane (Celgard 2400). The TiS_2-VF/Celgard membrane was dried in a vacuum oven at 50 °C for 20 h for further use. The mass loading of TiS_2 in TiS_2-VF/Celgard is about 0.504 mg cm^{-2}. A Super P modified separator (Super P/Celgard) was prepared similarly by replacing TiS_2 with Super P. To prepare TiS_2-SC/Celgard, 35 mg TiS_2 and 5 mg PVDF binder were dispersed in NMP to form a homogeneous slurry. The prepared slurry was then coated on a PP separator (Celgard 2400) and pressed using a roller press. After drying in a vacuum oven at 50 °C for 20 h, the TiS_2-SC/Celgard modified separator can be prepared.

Fabrication of the S cathode

Firstly, sulfur and KB were mixed at a mass ratio of 7 : 3 and heated in a sealed quartz tube at 155 °C for 20 h to prepare a positive electrode active material. The active material was mixed with Super-P and PVDF in a weight ratio of 7 : 2 : 1, and then dispersed in NMP to form a homogeneous slurry. Finally, the slurry was coated onto carbon-coated Al foil and dried at 60 °C under vacuum for 12 h.

Characterization methods

The crystal structure of the as-prepared materials was measured by X-ray diffraction (XRD, CuKα radiation, λ = 1.5418 Å). A scanning electron microscope (SEM, SU-70) and high-resolution transmission electron microscope (HR-TEM, JEOL, JEM-2100F) were used to characterize the morphology and elemental distribution of the samples. N_2 adsorption–desorption isotherms were measured on an adsorption device (Micromeritics ASAP2020) at 77 K. Thermogravimetric analysis curves were obtained with a thermal analyzer (TGA, TG209F1). X-ray photoelectron spectroscopy (XPS, Thermo Scientific ESCALAB 250XI) was used to analyze TiS_2. UV-Vis (Lambda

750) absorption spectra were performed to evalute the concentration of PSs.

Preparation of polysulfide solution and the adsorption experiment

5 mM Li_2S_6 solution was prepared by dissolving S and Li_2S with a molar ratio of 5 : 1 in a mixed solution of 1,2-dioxolane (DOL)/dimethoxymethane (DME) (v/v = 1 : 1). After vigorous stirring at 60 °C overnight, a dark yellow solution was obtained. To compare the adsorption performance of TiS_2 and Super P on LiPS, 50 mg TiS_2 powder and 50 mg Super P were added into 10 mL of 5 mM Li_2S_6 solution, respectively.

Assembly and measurements of symmetrical batteries

Electrodes for symmetrical batteries were manufactured in the absence of sulfur. Generally, the electrode material and PVDF binder were dispersed in NMP with a mass ratio of 4 : 1. The resulting slurry was then coated on Al foil using a doctor blade. After drying in a vacuum oven, an electrode disk with a diameter of 12 mm was punched out of the Al foil. These disks were used as the working and counter electrodes. The mass load of the active substance (TiS_2) is about 1.2 mg cm^{-2}. A mixture of Li_2S_6 (0.2 mol L^{-1}) and LiTFSI (1 mol L^{-1}) in DOL/DME (50 μL, 1 : 1 volume ratio) was used as the electrolyte. Cyclic voltammetry (CV) was carried out on the CHI660E electrochemical workstation at a scan rate of 1 mV s^{-1} in the potential range of −1.0–1.0 V *vs.* Li/Li^+. The electrochemical impedance spectrum (EIS) was recorded at an open circuit potential, applying a sinusoidal voltage with an amplitude of 10 mV.

Electrochemical measurement

Button-type (CR2032) Li–S batteries were assembled in a glove box with sulfur as the cathode, metallic lithium as the anode, Celgard or modified Celgard as the separator, and 1.0 M LiTFSI with 1 wt% $LiNO_3$ in DOL/DME as the electrolyte, respectively. A Neware constant current charge–discharge meter was used to collect charge–discharge data between 1.5 and 3.0 V at various current densities. The CV test was carried out on the CHI660E electrochemical workstation at a scan rate of 0.1 mV s^{-1} in the potential range of 1.5–3.0 V *vs.* Li/Li^+, and the EIS test was performed in the frequency range of 0.1 Hz–100 kHz.

3. Results and discussion

TiS_2 was prepared from titanium powder and sulfur powder by a simple solid-phase synthesis method.[27] First, the crystal structure of the material was investigated. Fig. 2a shows the XRD patterns of TiS_2 synthesized with different reaction durations, and all diffraction peaks can be ascribed to the typical hexagonal TiS_2 (JCPDS No.15-8853).[28] The two characteristic peaks at 15.6° and 34.2°, correspond to the (001) plane and (011) plane of TiS_2, respectively. XPS is used to characterize the chemical bonding configuration of the prepared TiS_2. Fig. 2b and c show the Ti 2p and S 2p XPS spectra of the TiS_2 nanosheet, respectively. The binding energy of 456.04 eV and 462.2 eV can be ascribed to the $2p_{1/2}$ and $2p_{3/2}$ orbitals of Ti in TiS_2,[29,30] while the binding energy of 458.62 eV and 464.3 eV can be ascribed to the $2p_{1/2}$ and $2p_{3/2}$ orbitals of Ti in Ti–O,[31] which indicate partial surface oxidation of TiS_2.[32] The S 2p spectrum with binding energies of 160.4 eV and 161.6 eV corresponds to the $2p_{3/2}$ and $2p_{1/2}$ orbitals of S in TiS_2, respectively.[30] The broader peak centered at around 168 eV is due to sulfate adsorbed on its surface.[33] According to the N_2 adsorption–desorption isotherm shown in Fig. S1a,† the BET specific surface area of TiS_2 is about 1.315 m^2 g^{-1}, which confirms that TiS_2 does not have a microporous structure.[34]

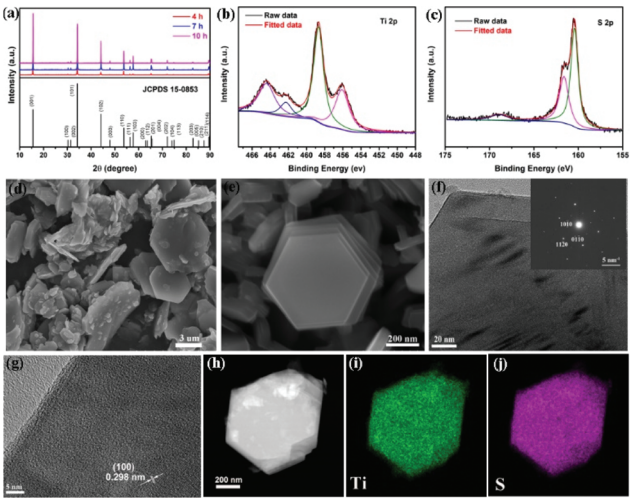

Fig. 2 (a) XRD patterns of TiS_2 synthesized with different reaction durations, (b) Ti 2p, and (c) S 2p XPS spectra of TiS_2. (d and e) SEM images of the prepared TiS_2; (f and g) high-resolution TEM images of TiS_2 with the corresponding FFT pattern in the inset. (h–j) Elemental mapping images of S and Ti in the selected region of TiS_2.

The morphology and microstructure of the prepared materials were analyzed by SEM and TEM. As shown in Fig. 2 (d and e) and Fig. S2,† micron-sized flake samples with regular hexagons can be observed, corresponding to the hexagonal crystal structure of TiS_2. The TEM image shows a layered structure (Fig. S1b†). HRTEM image (Fig. 2f) demonstrates the single-crystalline nature of TiS_2, and a lattice fringe of 2.98 Å corresponding to the (100) plane of the TiS_2 crystal (Fig. 2g). Selected electron diffraction (SAED) patterns of TiS_2 (Fig. 2g), demonstrates a hexagonal phase structure of TiS_2 with a crystal growth direction along the [1, 1, 2, 1] zone axis. Energy-dispersive X-ray element mapping images (Fig. 2h–j) show the uniform distribution of each element in TiS_2 nanoplates.

Vacuum filtration and slurry coating have been applied to prepare TiS_2/Celgard membranes which are denoted as TiS_2-VF/Celgard and TiS_2-SC/Celgard, respectively. The corresponding SEM images of Celgard, Super P/Celgard, and TiS_2/Clegard are shown in Fig. 3(a–d) and Fig. S3.† Celgard is a

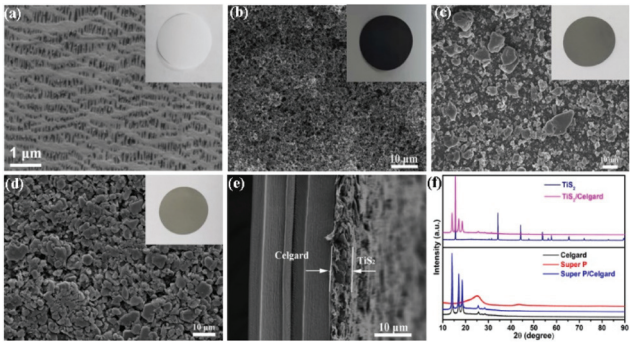

Fig. 3 SEM images of (a) Celgard, (b) Super P/Celgard, (c)TiS_2-SC/Celgard, and (d) TiS_2-VF/Celgard; (e) cross section image of TiS_2 layers in the TiS_2-VF/Celgard separator; and (f) XRD patterns of Super P, TiS_2, Celgard, Super P/Celgard and TiS_2/Celgard.

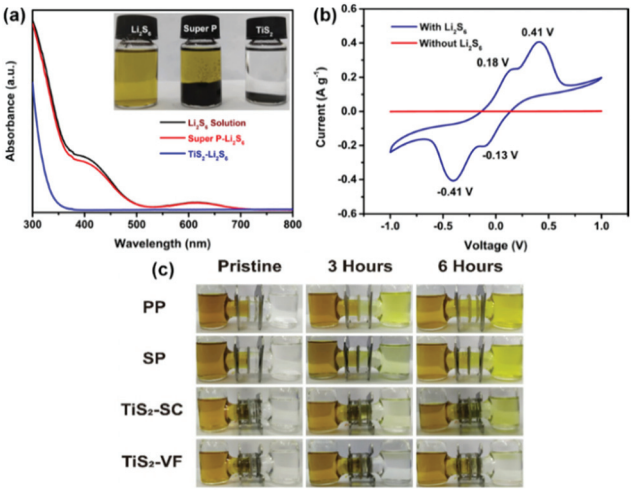

Fig. 4 (a) UV-vis spectra of the PS solution before and after being soaked in TiS_2, or Super P, with the colour change shown in the inset. (b) CV curves of TiS_2-based symmetric cells in electrolytes with and without the addition of Li_2S_6 at 1 mV s^{-1}; and (c) optical images of permeation tests for Celgard, Super P/Celgard, TiS_2-SC/Celgard and TiS_2-VF/Celgard separators.

macroporous membrane with a porosity of ~40% and a pore size of ~100 nm (Fig. 3a).

Due to the high surface area of nanocarbon particles, most of the surface holes in Super P/Celgard are covered (Fig. 3b). The surface of TiS_2-SC/Celgard prepared by the slurry coating method is relatively non-uniform (Fig. 3c), and the slow evaporation of solvents results in a loosely stacked film. TiS_2-VF/Celgard prepared by vacuum filtration has a more densely packed layer that fully covered the macropores of Celgard (Fig. 3d) with a layer thickness of 6 μm (Fig. 3e). The calculated loading of TiS_2 is about 0.504 mg cm^{-2}. Inset in Fig. 3 shows that the color changes from white to brass after modification with TiS_2. The modified separators have not shown fracture or exfoliation after repeated folding and reopening to 180°, which demonstrates the strong affinity of TiS_2 to Celgard (Fig. S4b†). Furthermore, Super P/Celgard has been prepared by vacuum filtration of Super P slurry on the Celgard 2400 membrane (Fig. S4a†). The crystal structures of the TiS_2/Celgard and Super P/Celgard were characterized by X-ray diffraction (XRD). The Super P/Celgard separator has the characteristic diffraction peaks of Celgard and the SEM and optical images shown in Fig. 3b prove that it is successfully modified by carbon. The TiS_2/Celgard separator contains characteristic peaks of TiS_2 and Celgard (the weak intensity is due to the low proportion), indicating the incorporation of crystalline TiS_2 on the surface of Celgard (Fig. 3f). XRD data indicated that neither vacuum filtration slurry nor the coating process change the crystal structure of TiS_2 or Celgard.

The static adsorption test was initially performed to test the adsorption capacity and chemical interaction between TiS_2 and PS species.[35,36] As shown in Fig. 4a, the same mass of Super P and TiS_2 were added to 5 mmol L^{-1} Li_2S_6. The color of the Li_2S_6 solution mixed with TiS_2 vanished after 20 hours of adsorption, and barely changed for those mixed with Super P. The static adsorption test indicates the stronger adsorption properties of TiS_2 toward PSs compared to porous carbon materials. UV-vis spectra of the samples (Fig. 4a) show adsorption peaks at 320, 410, and 620 nm, which can be ascribed to the S_6^{2-}, S_4^{2-}, and S_2^{2-} species, respectively.[37] The TiS_2 in Li_2S_6 has the lowest adsorption peaks for S_6^{2-}, S_4^{2-}, and S_2^{2-} species, which further confirms the better immobilization of PSs on TiS_2 than on porous carbon. CV tests for symmetric TiS_2 batteries were performed with and without the Li_2S_6 electrolyte at a scan rate of 1 mV s^{-1}. The TiS_2 electrode in the Li_2S_6 electrolyte shows relatively good reversibility (Fig. 4b), the peak at −0.41 V, 0.18 V, 0.41 V, and −0.13 V can be attributed to the oxidation of Li_2S_6, reduction of S_8 to Li_2S_6, continuous conversion of Li_2S_6 to Li_2S/Li_2S_2, and conversion reaction of Li_2S/Li_2S_2 to Li_2S_6, respectively.[38] The permeation of PSs through the modified membranes has been tested in H-shaped glass tubes with the coating layer of the separator facing the Li_2S_6 (0.02 M) solution, while the uncoated side is in contact with DME solvent (Fig. 4c). Celgard can barely prohibit the diffusion of PSs and the DME solution turned yellow after 3 hours. The Super P/Celgard and TiS_2-SC/Celgard-based H cells have shown the diffusion of PSs through the separators after 6 h. The TiS_2-VF/Celgard-based H cell has shown negligible permeation of PSs through the separator, indicating that TiS_2-VF/Celgard has the strongest PSs immobilization capacity among all the modified separators.

Li^+ diffusion is a key factor affecting the electrochemical performance of Li–S batteries. CVs of different modified separator-based cells at different scan rates were measured to calculate the lithium-ion diffusion rates. The calculation is according to the Randles–Sevcik equation (1)[39,40].

$$I_P = 2.69 \times 10^5 n^{1.5} A D_{Li^+}^{0.5} v^{0.5} C_{Li^+} \quad (1)$$

where D_{Li^+} stands for the Li^+ diffusion coefficient (cm^2 s^{-1}), I_p stands for the peak current in amps (A), n stands for the number of electrons participating in the electrochemical reaction (for Li–S batteries, n = 2), A stands for the electrode area

(1.13 cm^2 here), C_{Li^+} is the concentration of Li^+ (mol L^{-1}), and v stands for the scanning speed (V s^{-1}). The calculation of the Li^+ diffusion coefficient is based on the slope of the linear diagram of the peak current (I_p) to the square root of the scan rate ($v^{0.5}$). The second pair of CV curves was selected to measure the Li^+ diffusion coefficient. As shown in Fig. 5 and Fig. S5,† the cathodic peaks A and B at 1.8–2.1 V and 2.2–2.4 V, and the anodic peak C at around 2.4–2.6 V can be observed. The CV curves at different scan rates are plotted in Fig. 5a and Fig. S5(a–c),† and the linear fitting results are shown in Fig. 5b and Fig. S5(d–f).† The I_p is proportional to $v^{0.5}$ (Fig. 5b), regardless of the scan rates, indicating that the PS redox reaction is intrinsically a diffusion-controlled process. The Li^+ diffusion coefficient values for different separator-based Li–S batteries have been calculated from the slope of the fitted line. For batteries with Celgard and Super P/Celgard separators, the Li^+ diffusion coefficient values are D_{Li^+}(A1) = 1.54 × 10^{-9} cm^2 s^{-1}, D_{Li^+}(B1) = 2.72 × 10^{-9} cm^2 s^{-1}, and D_{Li^+}(C1) = 1.45 × 10^{-8} cm^2 s^{-1}; and D_{Li^+}(A2) = 8.7 × 10^{-10} cm^2 s^{-1}, D_{Li^+}(B2) = 1.3 × 10^{-9} cm^2 s^{-1}, and D_{Li^+}(C2) = 3.28 × 10^{-9} cm^2 s^{-1}, respectively. TiS2-SC/Celgard and TiS2-VF/Celgard separator-based cells have Li^+ diffusion coefficient values of DLi$^+$(A3) = 4.71 × 10^{-9} cm^2 s^{-1}, D_{Li^+}(B3) = 4.87 × 10^{-9} cm^2 s^{-1}, and D_{Li^+}(C3) = 3.81 × 10^{-8} cm^2 s^{-1}; and D_{Li^+}(A4) = 1.59 × 10^{-8} cm^2 s^{-1}, D_{Li^+}(B4) = 7.93 × 10^{-9} cm^2 s^{-1}, and D_{Li^+}(C4) = 4.68 × 10^{-8} cm^2 s^{-1}, respectively. Fig. 5c compares the Li^+ diffusion coefficient values of different separator-based batteries. The Li^+ diffusion coefficient of Super P/Celgard is lower than that of Celgard, and this can be caused by pore blockage due to the small size of Super P. Moreover, the Li^+ diffusion coefficient values of the TiS_2 modified separator-based batteries are higher than that of Celgard-based batteries. The larger size of TiS_2 than the pore size of Celgard enables the deposition of TiS_2 on the Celgard surface without blocking the pore channels of Celgard. TiS_2 as an adsorption matrix provides voids to accommodate redox materials and prevents the formation of an insulating layer. When applied as a coating layer, TiS_2 can form a homogeneous coating layer without blocking the pores of separators. The separator modification process also has key impacts on its electrochemical performance. TiS_2-VF/Celgard-based cells have a significantly larger Li^+ diffusion coefficient than TiS_2-SC/Celgard-based cells. Vacuum filtration quickly removes most of the solvents and forms a tightly packed film (Fig. 3d), while the slurry coating process involves gradual evaporation of solvents, which leaves a loosely packed film with numerous holes.

EIS has been measured to evaluate the Li^+ conductivity of the TiS_2/Celgard separator (Fig. 5d) with an evaluation methodology established in earlier reports.[41] The TiS_2-VF/Celgard separator has the highest Li^+ conductivity of 0.211 mS cm^{-1}, followed by TiS_2-SC/Celgard (0.141 mS cm^{-1}) and Super P/Celgard separators (0.132 mS cm^{-1}), and these are higher than the Celgard separator (0.179 mS cm^{-1}). The MacMullin number (N_M) defined as the ratio of the conductivity of the electrolyte to the electrolyte-containing separator can be used to analyze the porosity of the separator, with the following equation.[41]

$$N_M = \sigma_0/\sigma_e \quad (2)$$

where σ_0 and σ_e are the conductivities of electrolyte and separator containing electrolyte, respectively.

The conductivity of the electrolyte σ_0 (8.62 mS cm^{-1}) was determined using a conductivity meter at 25 °C. TiS_2-VF/Celgard, TiS_2-SC/Celgard, Super P/Celgard, and Celgard separators have N_M values of 41, 61, 65, and 50, respectively. These results indicate that the modification of separators does not significantly reduce the Li^+ conductivity.

EIS spectra of different separator-based electrochemical cells before and after cycling tests are shown in Fig. 6a and b with fitting circuits and results in Fig. 6c, and Table S1.†

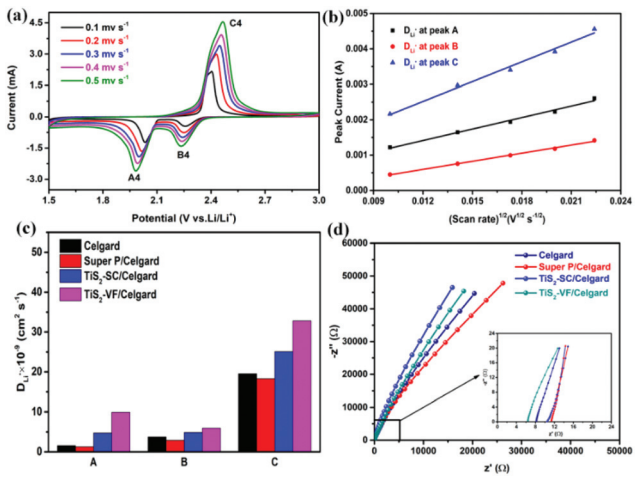

Fig. 5 Cyclic voltammograms of TiS_2-VF/Celgard-based batteries (a) and the linear fitting (b) in the voltage range of 1.5–3.0 V at 0.1, 0.2, 0.3, 0.4, and 0.5 mV s^{-1}. The Li^+ diffusion coefficient values of the Celgard, Super P/Celgard, TiS_2-SC/Celgard, and TiS_2-VF/Celgard separator-based batteries (c), and their corresponding electrochemical impedance plots for the measurement of Li-ion conductivity (d).

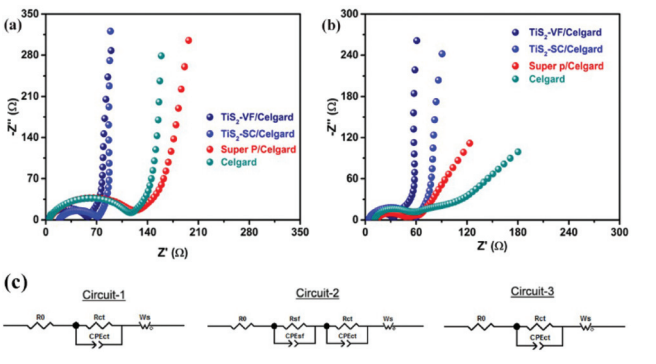

Fig. 6 EIS spectra of Celgard, Super P/Celgard, TiS_2-SC/Celgard, and TiS_2-VF/Celgard-based Li–S batteries (a) before and (b) after the cycling test, and (c) corresponding equivalent circuit diagram. Equivalent circuit-1 stands for all the batteries before cycling tests, circuit-2 represents Celgard- and Super P/Celgard-based batteries after cycling tests, and circuit-3 refers to TiS_2-SC/Celgard- and TiS_2-VF/Celgard-based Li–S batteries after cycling tests.

Before the cycling test, all the cells have shown semicircles in the high-frequency region, which corresponds to the charge transfer resistance (R_{ct}) and resistance of the electrolyte and electrode contact (R_0). The resistance in the low-frequency region of the diagonal line is related to the Warburg impedance (W_s). The R_{ct} for TiS_2-SC/Celgard and TiS_2-VF/Celgard-based cells are 52.46 Ω and 57.01 Ω, respectively, both lower than those of Super P/Celgard (117.66 Ω) and Celgard (110.25 Ω). The semicircle in the high frequency region (R_{sf}) is related to the formation of an insulating layer of solid Li_2S_2/Li_2S between the separator and cathode, while the semicircle in the middle frequency region (R_{ct}) is related to the charge transfer resistance (Fig. 6c). After cycling, Celgard and Super P/Celgard-based Li–S cells exhibit two semicircles in the high- and middle-frequency regions, which correspond to the insulating layer composed of PSs on the surface of the Li-anode, and the charge transfer resistance, respectively. TiS_2-SC/Celgard and TiS_2-VF/Celgard-based Li–S batteries have only one semicircle in the high-frequency region, indicating the suppressed PS migration from the cathode to anode. The TiS_2-VF/Celgard-based battery has the smallest R_{ct} (Table S1†), which is a result of the intrinsic conductivity of TiS_2, indicating that the battery reaction kinetics is accelerated.

The physicochemical and electrochemical characterization has shown that the TiS_2/Celgard separator is an ideal ion sieve, which can selectively transfer lithium ions while effectively preventing undesired PS shuttling. Standard CR2032 type button cells have been assembled with Ketjen Black (KB) and sulfur mixture as the cathode (KB/S), and Li metal as the anode. KB is uniformly mixed with sulfur, as seen from the SEM image and the corresponding elemental mapping (Fig. S6a–c†), and XRD pattern (Fig. S6d†) indicates a uniform mixture of KB with sulfur without severe aggregation or change of the crystal structure. TGA data indicate that KB/S powder has a sulfur ratio of 72 wt% (Fig. S6e†), corresponding to a sulfur mass ratio of ~50% in KB/S that was coated on Al foil.

The as-assembled Li–S batteries have a sulfur loading of ~1.8 mg cm^{-2}. Fig. S7a† shows that a typical CV curve of a TiS_2-VF/Celgard-based Li–S battery has two well-defined peaks at 2.25 V and 2.01 V which represent the reduction of elemental sulfur to soluble higher order PSs (Li_2S_n, $4 \leq n \leq 8$) and solid lithium sulfide (Li_2S_2/Li_2S), respectively.[42,43] In the subsequent anode scan, an oxidation peak at 2.43 V appears, corresponding to the electrochemical conversion of intermediate polysulfide PSs from Li_2S_2/Li_2S to S_8. The following CV curves almost overlapped with the 2nd cycle, implying good stability and reversibility of the battery. Comparing the CV curves of four batteries with different separators (Fig. 7a) it was found that TiS_2-VF/Celgard-based battery has a lower oxidation potential and higher reduction potential than those of the other three types of batteries, indicating a reduced electrochemical polarization and fast kinetics of Li–S batteries. Constant-current charge/discharge of battery with the TiS_2-VF/Celgard modified separator was carried out at the constant current rate of 0.5 C (Fig. S7b†).

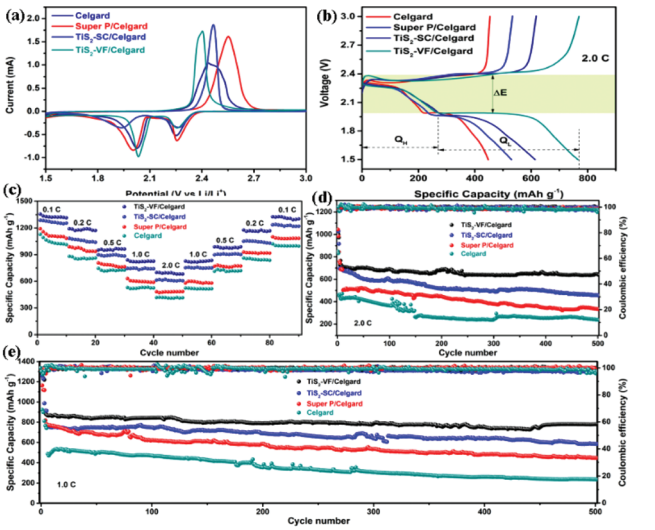

Fig. 7 (a) CV at a scan rate of 0.1 mV s^{-1}, (b) GCD curves, (c) rate performance from 0.1 to 2 C, and cycle life measurements at (d) 2 C and (e) 1 C for batteries with Celgard, Super P/Celgard, Tis_2-SC/Celgard and Tis_2-VF/Celgard separators.

The rate performance comparison of four types of separator-based batteries at different current densities from 0.1 C to 2 C is displayed in Fig. 7c. TiS_2-VF/Celgard-based batteries have an initial discharge specific capacity of 1352.8 mA h g^{-1} at 0.1 C, and specific capacities of 1196.8, 968.7, 833.6, and 713.2 mA h g^{-1} at 0.2, 0.5, 1 and 2 C. After a high rate GCD test, the specific capacity of TiS_2-VF/Celgard-based batteries was maintained at 1320.5 mA h g^{-1} at 0.1 C, indicating the high reversibility of the battery. TiS_2-VF/Celgard-based batteries have the highest low rate capacity and the best capacity retention at large GCD rates among the four types of separator-based batteries. For example, Super P/Celgard-based batteries have a specific capacity of 1157.4 mA h g^{-1} at 0.1 C, and only 480.1 mA h g^{-1} is retained at 2 C. The modified separator-based batteries have a higher reversible capacity and better rate performance than that of Celgard-based batteries. Among these types of batteries, the TiS_2-VF/Celgard exhibits the best rate performance, indicating the suppression of the PS shuttling effect without reducing the Li^+ diffusion efficiency. GCD curves of the four types of batteries at different current rates are shown in Fig. S8(a–d).† TiS_2-VF/Celgard-based batteries have shown smaller polarization than other types of batteries with a high voltage of discharge, indicating fast electrochemical kinetics towards PS redox reaction.

The cycling performance of various separator-based Li–S batteries at high current rates of 1 C and 2 C are shown in Fig. 7(d and e). The fluctuation of the cycle curve might be due to the environmental temperature change, which influences the electrolyte mobility, ionic conductivity, and electrochemical kinetics. After 500 cycles at 1 C, the capacities of Celgard-, Super P/Celgard-, TiS_2-SC/Celgard-, and TiS_2-VF/Celgard-based Li–S batteries are 236.2, 741.3, 811.2, and 887.3 mA h g^{-1}, respectively. Super P/Celgard- and TiS_2-SC/

Celgard-based batteries have discharge capacities of 741.3 and 811.2 mA h g^{-1} in the first cycle, and 445.8 and 584.5 mA h g^{-1} discharge capacities are retained after 500 cycles, with an average capacity loss of 0.079% and 0.056% per cycle, respectively. Celgard-based batteries have fast capacity decay at a high discharge current, indicating that the mesoporous PP separator is not applicable for Li–S batteries. TiS_2-VF/Celgard-based Li–S batteries have the highest capacity retention of 887.3 mA h g^{-1} after 500 cycles at 1 C, corresponding to an average attenuation of 0.024% per cycle. Moreover, the same trend has been observed for 4 types of separator-based batteries, TiS_2-VF/Celgard-based batteries have the highest capacity of 646.6 mA h g^{-1} after 500 cycles at 2 C, followed by TiS_2-SC/Celgard-, Super P/Celgard-, and Celgard-based batteries, which are 462.1, 342.2 and 237.5 mA h g^{-1}, respectively. The electrochemical performance of the TiS_2-VF/Celgard-based batteries is comparable and even superior to the recent reports of Li–S batteries which used high-performance modified separators (Table S2†).

The cycling performance of the four separator-based batteries at a high current rate of 2 C is shown in Fig. 7d. The initial discharge capacity of the TiS_2-VF/Celgard separator battery is 771.6 mA h g^{-1}. TiS_2-VF/Celgard-based batteries have the highest capacity retention ratio of 83%, far exceeding those of Li–S batteries with Celgard reference group (52%), Super P/Celgard (66%) and TiS_2-SC/Celgard (65%) separators. The electrochemical measurements of modified separators in Li–S cells further indicate the more efficient immobilization of PSs by the TiS_2 layer, and vacuum filtration has been validated as a better modification process than slurry coating.

The GCD curves of various separator-based batteries at 0.2 C and 2 C are further analyzed to understand the capacity contribution and energy storage mechanism (Fig. S10a† and Fig. 7b). TiS_2-VF/Celgard-based batteries have much lower voltage hysteresis with a lower voltage gap between oxidation and reduction platforms (ΔE) than Celgard-, Super P/Celgard-, and TiS_2-SC/Celgard-based batteries, indicating a lower resistance and faster electrochemical redox reactions. Low voltage hysteresis helps improve the energy efficiency, which is one of the key indicators for sustainable large-scale energy storage systems. Q_L/Q_H is defined as the peak area ratio associated with the formation of Li_2S, and PSs can be used to estimate the capacity contribution of electrochemical processes.[37,44] At a 0.2 C rate, the collection coefficients of batteries with a Celgard, Super P/Celgard, TiS_2-SC/Celgard, and TiS_2-VF/Celgard separator are 1.59, 1.54, 1.78, and 1.99, respectively, and have not shown significant differences. The four types of batteries have shown distinct differences at a high rate of 2 C, with collection coefficients of 0.81, 1.42, 1.15, and 1.84 for batteries with a Celgard, Super P/Celgard, TiS_2-SC/Celgard, and TiS_2-VF/Celgard separator. This indicates the TiS_2-VF/Celgard can more effectively inhibit the polysulfide shuttle effect and promote the reduction of PSs. Ragone plots of batteries with different modified separators are shown in Fig. S10b.† The battery with TiS_2-VF/Celgard separator has a high power density of 1.51 kW kg^{-1} and a high energy density of 311 W h kg^{-1} at 2 C, which is significantly higher than those of batteries with Celgard, Super P/Celgard, TiS_2-SC/Celgard, which are 173 W h kg^{-1}, 201 W h kg^{-1}, and 252 W h kg^{-1}, respectively, at a current density of 2 C.

At a low current density of 0.1 C, TiS_2-VF/Celgard-based cells show a high energy density of greater than 610 W h kg^{-1}, demonstrating their excellent energy storage performance. Benefiting from the efficient immobilization and electrochemical redox of PSs, low polarization also endows TiS_2-VF/Celgard-based batteries with high capacity at high rates, and improved electrochemical stability. As a modification layer of separators, TMDs represented by TiS_2 not only efficiently immobilize PSs, but also improves charge transfer kinetics and reduces the electrochemical polarization and delivers high Li^+ conductivity and low charge transfer resistance, hence a high energy density can be achieved.

4. Conclusions

In summary, a scalable, fast solid-phase synthesis method has been applied to synthesize single-crystalline TiS_2 microplates. As an ion-selective modification layer for commercially available separators, TiS_2 efficiently prohibits the shuttling of PSs through separators which maintains high Li^+ conductivity and enables fast diffusion of Li^+; therefore, a high energy density and long cycling stability can be achieved. The TiS_2 modified Celgard layer not only is a physical barrier which prohibits the diffusion of PSs, but also shows strong chemisorption and electrocatalysis towards PS, which promotes the fast and reversible conversion of PSs. At a high discharge rate of 2 C, Li–S batteries with a TiS_2-VF/Celgard separator has an initial capacity of 771.6 mA h g^{-1}, and an energy density as high as 311 W h kg^{-1}. After 500 cycles, the capacity retention for TiS_2-VF/Celgard-based batteries is 645.6 mA h g^{-1}, which is equivalent to 0.033% of capacity loss in each cycle. Moreover, vacuum filtration for separator modification has been validated as a more advanced process over slurry coating due to the formation of the more densely packed film in a fast solvent removal process. This work has manifested the promising application of TMDs as a modifier of conventional commercially available separators for high energy density and high cycle life Li–S batteries.

Conflicts of interest

There are no conflicts to declare.

Acknowledgements

The work is supported by the National Natural Science Foundation of China (Grant No. 51773171) and the CAS Pioneer Hundred Talents Program. The authors acknowledge Prof. Jun Xu for advice in the electrochemical test; the authors

acknowledge Dr Yun Yang for XRD, Mr Yange Wang for SEM, Mr Jinming Wang for TEM, and Mr Xiuming Zhang for spectroscopic measurements, respectively. The authors also acknowledge technical support from Wanli Li, Guodong Zhang, and Kai Chen.

Notes and references

1 R. Fang, S. Zhao, Z. Sun, D. W. Wang, H. M. Cheng and F. Li, *Adv. Mater.*, 2017, **29**, 1606823.
2 P. G. Bruce, S. A. Freunberger, L. J. Hardwick and J.-M. Tarascon, *Nat. Mater.*, 2011, **11**, 19–29.
3 Y. Wang, X. Huang, S. Zhang and Y. Hou, *Small Methods*, 2018, **2**, 1700345.
4 A. Manthiram, Y. Fu, S. H. Chung, C. Zu and Y. S. Su, *Chem. Rev.*, 2014, **114**, 11751–11787.
5 F. Yi, H. Ren, J. Shan, X. Sun, D. Wei and Z. Liu, *Chem. Soc. Rev.*, 2018, **47**, 3152–3188.
6 G. Zhang, Z.-W. Zhang, H.-J. Peng, J.-Q. Huang and Q. Zhang, *Small Methods*, 2017, **1**, 1700134.
7 J. Zhang, H. Huang, J. Bae, S.-H. Chung, W. Zhang, A. Manthiram and G. Yu, *Small Methods*, 2018, **2**, 1700279.
8 C. Li, Z. Xi, D. Guo, X. Chen and L. Yin, *Small*, 2018, **14**, 1701986.
9 S. Bai, K. Zhu, S. Wu, Y. Wang, J. Yi, M. Ishida and H. Zhou, *J. Mater. Chem. A*, 2016, **4**, 16812–16817.
10 X. Ni, T. Qian, X. Liu, N. Xu, J. Liu and C. Yan, *Adv. Funct. Mater.*, 2018, **28**, 1706513.
11 Y. C. Jeong, J. H. Kim, S. Nam, C. R. Park and S. J. Yang, *Adv. Funct. Mater.*, 2018, 1707411, DOI: 10.1002/adfm.201707411.
12 G. Zhou, S. Pei, L. Li, D. W. Wang, S. Wang, K. Huang, L. C. Yin, F. Li and H. M. Cheng, *Adv. Mater.*, 2014, **26**, 625–631, 664.
13 Z. Wang, J. Zhang, Y. Yang, X. Yue, X. Hao, W. Sun, D. Rooney and K. Sun, *J. Power Sources*, 2016, **329**, 305–313.
14 C.-H. Chang, S.-H. Chung and A. Manthiram, *J. Mater. Chem. A*, 2015, **3**, 18829–18834.
15 H. Wei, J. Ma, B. Li, Y. Zuo and D. Xia, *ACS Appl. Mater. Interfaces*, 2014, **6**, 20276–20281.
16 Z. Zhang, Y. Lai, Z. Zhang, K. Zhang and J. Li, *Electrochim. Acta*, 2014, **129**, 55–61.
17 W. Li, J. Hicks-Garner, J. Wang, J. Liu, A. F. Gross, E. Sherman, J. Graetz, J. J. Vajo and P. Liu, *Chem. Mater.*, 2014, **26**, 3403–3410.
18 X. Xu, W. Liu, Y. Kim and J. Cho, *Nano Today*, 2014, **9**, 604–630.
19 C. Jiang, M. Tang, S. Zhu, J. Zhang, Y. Wu, Y. Chen, C. Xia, C. Wang and W. Hu, *Angew. Chem., Int. Ed.*, 2018, **57**, 16072–16076.
20 J.-Q. Huang, B. Zhang, Z.-L. Xu, S. Abouali, M. A. Garakani, J. Huang and J.-K. Kim, *J. Power Sources*, 2015, **285**, 43–50.
21 R. H. Friend and A. D. Yoffe, *Adv. Phys.*, 1987, **36**, 1–94.
22 S. Z. Butler, S. M. Hollen, L. Cao, Y. Cui, J. A. Gupta, H. R. Gutierrez, T. F. Heinz, S. S. Hong, J. Huang, A. F. Ismach, E. Johnston-Halperin, M. Kuno, V. V. Plashnitsa, R. D. Robinson, R. S. Ruoff, S. Salahuddin, J. Shan, L. Shi, M. G. Spencer, M. Terrones, W. Windl and J. E. Goldberger, *ACS Nano*, 2013, **7**, 2898–2926.
23 K. Sun, M. Fu, Z. Xie, D. Su, H. Zhong, J. Bai, E. Dooryhee and H. Gan, *Electrochim. Acta*, 2018, **292**, 779–788.
24 R. Winter and P. Heitjans, *J. Phys. Chem. B*, 2001, **105**, 6108–6115.
25 S. Pan, Z. Yin, Q. Cheng, G. Zhang, X. Yu, Z. Pan, H. Rao and X. Zhong, *J. Alloys Compd.*, 2020, **832**, 154947.
26 X. Huang, J. Tang, B. Luo, R. Knibbe, T. Lin, H. Hu, M. Rana, Y. Hu, X. Zhu, Q. Gu, D. Wang and L. Wang, *Adv. Energy Mater.*, 2019, **9**, 1901872.
27 Z. Hu, Z. Tai, Q. Liu, S.-W. Wang, H. Jin, S. Wang, W. Lai, M. Chen, L. Li, L. Chen, Z. Tao and S.-L. Chou, *Adv. Energy Mater.*, 2019, **9**, 1803210.
28 H. Tao, M. Zhou, R. Wang, K. Wang, S. Cheng and K. Jiang, *Adv. Sci.*, 2018, **5**, 1801021.
29 M. G. Faba, D. Gonbeau and G. Pfister-Guillouzo, *J. Electron Spectrosc. Relat. Phenom.*, 1995, **73**, 65–80.
30 H. Martinez, C. Auriel, D. Gonbeau, M. Loudet and G. Pfister-Guillouzo, *Appl. Surf. Sci.*, 1996, **93**, 231–235.
31 D. Y. Oh, Y. E. Choi, D. H. Kim, Y.-G. Lee, B.-S. Kim, J. Park, H. Sohn and Y. S. Jung, *J. Mater. Chem. A*, 2016, **4**, 10329–10335.
32 A. Iwabuchi, K. C. Choo and K. Tanaka, *J. Phys. Chem. B*, 2004, **108**, 10863.
33 M. R. Bayati, A. Z. Moshfegh and F. Golestani-Fard, *Appl. Catal., A*, 2010, **389**, 60–67.
34 Y. Zhao, W. Cai, Y. Fang, H. Ao, Y. Zhu and Y. Qian, *ChemElectroChem*, 2019, **6**, 2231–2237.
35 A. Schneider, J. Janek and T. Brezesinski, *Phys. Chem. Chem. Phys.*, 2017, **19**, 8349–8355.
36 Z. W. Seh, J. H. Yu, W. Li, P. C. Hsu, H. Wang, Y. Sun, H. Yao, Q. Zhang and Y. Cui, *Nat. Commun.*, 2014, **5**, 5017.
37 Z. Xiao, Z. Yang, L. Wang, H. Nie, M. Zhong, Q. Lai, X. Xu, L. Zhang and S. Huang, *Adv. Mater.*, 2015, **27**, 2891–2898.
38 H. Lin, L. Yang, X. Jiang, G. Li, T. Zhang, Q. Yao, G. W. Zheng and J. Y. Lee, *Energy Environ. Sci.*, 2017, **10**, 1476–1486.
39 J.-Q. Huang, T.-Z. Zhuang, Q. Zhang, H.-J. Peng, C.-M. Chen and F. Wei, *ACS Nano*, 2015, **9**, 3002.
40 Z. A. Ghazi, X. He, A. M. Khattak, N. A. Khan, B. Liang, A. Iqbal, J. Wang, H. Sin, L. Li and Z. Tang, *Adv. Mater.*, 2017, **29**, 1606817.
41 T.-H. Cho, M. Tanaka, H. Onishi, Y. Kondo, T. Nakamura, H. Yamazaki, S. Tanase and T. Sakai, *J. Power Sources*, 2008, **181**, 155–160.
42 H.-J. Peng, J.-Q. Huang, M.-Q. Zhao, Q. Zhang, X.-B. Cheng, X.-Y. Liu, W.-Z. Qian and F. Wei, *Adv. Funct. Mater.*, 2014, **24**, 2772–2781.
43 X. Wang, G. Li, J. Li, Y. Zhang, A. Wook, A. Yu and Z. Chen, *Energy Environ. Sci.*, 2016, **9**, 2533–2538.
44 Z. Xiao, Z. Yang, L. Zhang, H. Pan and R. Wang, *ACS Nano*, 2017, **11**, 8488–8498.